



HAL
open science

Ambient Seismic Noise Imaging of the Lowermost Mantle Beneath the North Atlantic Ocean

Lise Retailleau, Pierre Boué, Lei Li, Michel Campillo

► **To cite this version:**

Lise Retailleau, Pierre Boué, Lei Li, Michel Campillo. Ambient Seismic Noise Imaging of the Lowermost Mantle Beneath the North Atlantic Ocean. *Geophysical Journal International*, 2020, 222 (2), pp.1339-1351. 10.1093/gji/ggaa210 . hal-02928287

HAL Id: hal-02928287

<https://hal.univ-grenoble-alpes.fr/hal-02928287>

Submitted on 2 Sep 2020

HAL is a multi-disciplinary open access archive for the deposit and dissemination of scientific research documents, whether they are published or not. The documents may come from teaching and research institutions in France or abroad, or from public or private research centers.

L'archive ouverte pluridisciplinaire **HAL**, est destinée au dépôt et à la diffusion de documents scientifiques de niveau recherche, publiés ou non, émanant des établissements d'enseignement et de recherche français ou étrangers, des laboratoires publics ou privés.

Ambient Seismic Noise Imaging of the Lowermost Mantle Beneath the North Atlantic Ocean

Lise Retailleau^{1,2*}, Pierre Boué³, Lei Li³ and Michel Campillo³

¹ Department of Geophysics, Stanford University, Stanford, California, USA.

² Now at Observatoire Volcanologique du Piton de la Fournaise, Institut de Physique du Globe de Paris, CNRS, UMR 7154-Sismologie, La Plaine des Cafres, La Réunion, France

³ Université Grenoble Alpes, Univ. Savoie Mont Blanc, CNRS, IRD, IFSTTAR, ISTerre, 38000 Grenoble, France.

In press Geophysical Journal International (accepted April 27, 2020)

*Corresponding author: Lise Retailleau (retailleau@ipgp.fr)

Key Points

- We extract body waves that propagated in the lower mantle of the Earth using ambient noise correlations
- Using array analysis we recover a first image of the Core-Mantle-Boundary using ambient noise correlations
- Our study highlights strong lower-mantle heterogeneities underneath the North Atlantic Ocean

Keywords

Ambient noise correlations, body waves, Core-Mantle-Boundary

Abstract

Body waves can be extracted from correlation functions computed from seismic records even at teleseismic distances. Here we propose to use P and PcP waves from the secondary microseism frequency band that are propagating between Europe and the Eastern US to image the Core-Mantle Boundary (CMB) and D" structure beneath the North Atlantic. This study presents the first 3D image of the lower mantle obtained from ocean-generated microseism data. Robustness of our results is evaluated by comparing images produced by propagation in both directions. Our observations reveal complex patterns of lateral and vertical variations of P-wave reflectivity with a particularly strong anomaly extending upward in the lower mantle up to 2600km deep. We compare these results with synthetic data and associate this anomaly to a Vp velocity increase above the CMB. Our image aims at promoting the study of the lower mantle with microseism noise excitations.

1. Introduction

Constraining the chemical, thermal and mechanical processes that occur in the deep mantle is critical to better understand the Earth's past and future dynamics. One of the Earth's major discontinuities, the Core-Mantle-Boundary (CMB) is conventionally located at 2981km depth. It marks the limit between the turbulent flow of liquid molten iron alloy in the outer core and the viscous silicate rocks of the lower mantle. It is also, with the Earth's surface, the region that shows the most contrasts in density, viscosity, and elastic wave properties. The lowermost mantle, usually defined as the region between the CMB and 200-300 km above it and designated as the D" layer (Bullen 1949), is known to be a complex and discontinuous shell that plays a significant role in fundamental geodynamic processes such as mantle convection (Lay 2007) and dynamo effect operating in the outer-core (Glatzmaier et al. 1999). The D" layer is generally associated with a thermal boundary layer produced by heat fluxing from the much hotter core to the colder lower mantle. A simple thermal discontinuity is not the only candidate that could lead to a seismic wave reflection/diffraction and multiple factors and combinations of factors were rapidly proposed in the literature to explain seismic observations

such as a presence of sinking slab debris or thermo-chemical layering (Boyet and Carlson 2005, Herlund & McNamara 2015). The presence of subducted material in the deep mantle as a possible origin for plumes and hotspots has been debated for several years (Workman and Hart 2005). In contrast, laboratory and computational mineral physics experiments demonstrated the existence of a phase transition from perovskite to a denser post-perovskite at pressure and temperature close to lower mantle conditions (see Cobden et al., 2015, for a review). But even if this strong mineral physics argument seems compatible with most seismic observations, the consensus is moving towards a multi-factor explanation. Consequently, multidisciplinary analyses have been carried out for the past decades to obtain reasonable structural and geodynamic models of the deep mantle and outermost core. To construct a realistic picture, one should use all available inputs from each of these fields to deal with inherent tradeoffs and/or uncertainties of each method.

Seismology plays a major role by bringing direct measurements of elastic properties of the Earth structure with depth. Numerous global tomographic inversions have defined the large-scale structures of the lowermost mantle using various seismic datasets: body wave arrival times, normal modes and/or surface wave dispersion (e.g. Mégnin and Romanowicz, 2000; Panning and Romanowicz, 2006; Houser et al., 2008; Kustowski et al., 2008; Simmons et al., 2009; Ritsema et al., 2011; Lekic et al., 2012; Moulik & Ekström, 2014; French and Romanowicz, 2015; Koelemeijer et al. 2016; Durand et al., 2016; Garnero et al., 2016; Durand et al., 2017). These studies have highlighted the presence of two Large Low Shear Velocity Provinces (LLSVPs) beneath Africa and the Pacific. Given the input data and the inversion methods, these tomographic models are usually depicting smooth deep Earth structures. The lack of resolution within the lower mantle (generally >1000 km) prevents consensual conclusions on the fine structures and more importantly on physico-chemical processes. Seismic velocities are obviously important attributes for identifying the physical nature of heterogeneities, but velocity contrasts alone are really informative only if the spatial geometry of these heterogeneities is properly constrained across scales. Tomographic images are too

smooth to reveal sharp details and other constraints are needed. For instance, better azimuthal coverage of the illumination of the deep mantle (together with a denser ray coverage) helps to measure the anisotropy and better constrain mineralogical structure at depth (Cobden et al. 2015). Observations and modeling of various specific seismic phases in local regions of the globe have been critical to identifying smaller-scale heterogeneities such as Ultra Low Velocity Zones (ULVZ, Williams and Garnero, 1996) and small-scale (<10 km) scatterers (e.g. Rost and Earle, 2010). Using high frequency scattered/reflected P- and S-waves is one of the best ways to detect and probe these heterogeneities (e.g. Earle and Shearer, 1997). The top of the D'' discontinuity has been extensively studied in various places around the globe (e.g., Lay and Helmberger, 1983; Thomas et al., 2004a, 2004b, Gassner et al., 2015). Overviews on the lower mantle and D'' can be found in Wyssession et al. (1998), Garnero (2000), Lay and Garnero (2011) and Lay (2015).

Deep-Earth seismology surveys rely on moderate to large earthquakes to generate impulsive and sufficiently energetic seismic waves that can interact with the fine structure of the Earth and finally reach a sensor at the Earth's surface. Seismologists use various types of wave travel-paths to optimize the Earth coverage, but the regions probed by these waves are ultimately controlled and limited by the earthquake distribution. However, we note the significant effort and constant improvement made to exploit the signals from the earthquakes as fully as possible. For instance, Lai et al. (2019) developed a method to build high-quality travel time dataset including multiply reflected waves such as SSS and ScSScS waves. If we look carefully at previous studies made in our region of interest, which is beneath the North Atlantic, the lower mantle was probed by few studies using earthquakes mostly distributed in South and Central America. Closer to our study, Yao et al. (2015) observed clear S wave reflected waves (SdS) related to D'' under the North Atlantic Ocean from a single earthquake in the South of Spain and measured on an array of sensors in the USA (transportable USArray). They concluded the existence of a ~300 km thick D'' with a positive velocity jump ranging from 2 to 4%, matching previous studies in neighboring regions. Durand et al (2019)

recently extended that study by detecting both SdS and PdP reflections. This latest article also concluded that the D" layer region beneath the North Atlantic Ocean shows a strong positive velocity jump (ranging from 2.7 to 3.8%) at 300 km above the CMB with significant lateral variations. A recent review of previous studies in this region can be found in Li et al. (2019). This kind of studies would benefit significantly from an increase in the number of reflection points at the CMB and above, with a broader offset and azimuthal coverage, which would help constrain the 3D geometry of the observed discontinuity.

In this study, we focus on specific types of seismological data that are retrieved from ambient seismic noise. At period band longer than 1s the ambient seismic noise is linked mostly to the interactions between the ocean and the solid Earth (Longuet-Higgins, 1950; Hasselmann, 1963). The strongest energy, in the 3 to 10 s period band, is called secondary microseism (Kedar et al. 2008, Ardhuin et al., 2011, Hillers et al., 2012; Stutzmann et al 2012). It is generated by the non-linear interaction between oceanic waves traveling at the same period with opposite directions. This interaction occurs either within a storm, between two storms, or when ocean waves generated by a storm propagate to a coast and are reflected back in the direction of the storm. The resulting standing wave generates a pressure field at the bottom of the ocean that is converted to seismic waves.

The permanent weak and complex wavefield resulting from these oceanic sources can be turned to useful deterministic signals using the correlation operator (seismic interferometry). Noise-based seismic methods constitute a valuable supplement to earthquake data since they are mostly constrained by the sensor locations (Shapiro and Campillo, 2004, Shapiro et al., 2005, Sabra et al., 2005). Their application was first limited to the uppermost layers of the Earth, as surface waves dominate the extracted signals. However, it was demonstrated that crustal body-wave reflections (Zhan et al., 2010; Ruigrok et al., 2011; Poli et al., 2012a) can be extracted from ambient noise correlations. Poli et al. (2012b) then made a first observation of the upper mantle discontinuities (at 410 and 660 km of depth) using a similar method across

a cratonic region. Following these observations, different studies generalized the methodology to teleseismic phase detections (Nishida, 2013, Lin et al., 2013b; Boué et al., 2013, 2014). In these studies, it was shown that the retrieved seismic phases carried structural information of the deep Earth. Poli et al. (2015) successfully identified a D'' reflector at 2530 km depth by extracting a PdP phase on correlation functions computed between Finland and Japan. While the Signal to Noise Ratio (SNR) recovered from correlation of ambient noise is lower, it benefits from array processing on both the source and receiver side (as will be developed here). This new class of signals has been proven to be a good supplement to earthquake data for deeper and deeper targets. In parallel, studies have extracted body wave sources of seismic signals linked to oceanic activity in the ambient noise (Gerstoft et al., 2008, Zhang et al., 2010, Landès et al., 2010, Retailleau and Gualtieri, 2019, Li et al., 2020). These studies lead the way to a better understanding of the body waves observed by correlation methods and thus to their better use for imaging. Other studies are developing processes to invert ambient noise correlations for the structure and the sources simultaneously (Fichtner et al 2016, Sager et al 2018). Alongside the development of body wave retrievals from ocean and solid Earth interactions (Nishida, 2013, Boué et al., 2013), different studies point out the possibility to use longer period body waves retrieved from large earthquake late coda arrivals (eg. Boué et al., 2014; Huang et al., 2015; Wu et al., 2018; Pham et al., 2018). This particular method usually shows a richer wavefield with very good SNR as compared to a noise-based approach, but one should be careful because the correlation does not necessarily converge toward the natural Earth impulse response (Poli et al., 2017; Kennett and Pham, 2018). As compared with noise-based correlations derived from a ballistic wavefield emanating from Ocean waves, signals retrieved from coda waves between station pairs are less straightforward to exploit to image 3D heterogeneities of the Earth. Nonetheless, coda wave correlations have proven to be very efficient to extract the weak signature of velocity deviation from 1D reference models for the deepest part of the Earth (Tkalčić and Pham, 2018). Wang and Tkalčić (2020) tend to demonstrate, with very promising synthetic examples, that this type of signals could also be used to resolve 3D structures of the inner core.

In the present article, we produce an original 1250 km x 950 km aperture (at the CMB 680 km x 520 km) image of the deep mantle beneath the North Atlantic Ocean using P and PcP body waves extracted from correlations of the secondary microseism computed from about 900 stations in the United States (US) and Europe (Figure 1). This area is located North of the region studied by Weber and Körnig (1992) and East of the previously mentioned studies by Yao et al. (2015) and Durand et al. (2019). These two study areas are represented in Figure 1. We first show that P and PcP phases are observed on both the causal and anticausal part of the correlation functions in the secondary microseism period band (3-8 seconds) after stacking a 1-year dataset. Following this, we use this very large correlation dataset (about 100.000 paths, i.e. turning points at depth) to constrain regional reflectivity variations in the few hundreds of kilometers around the CMB using a double-array analysis.

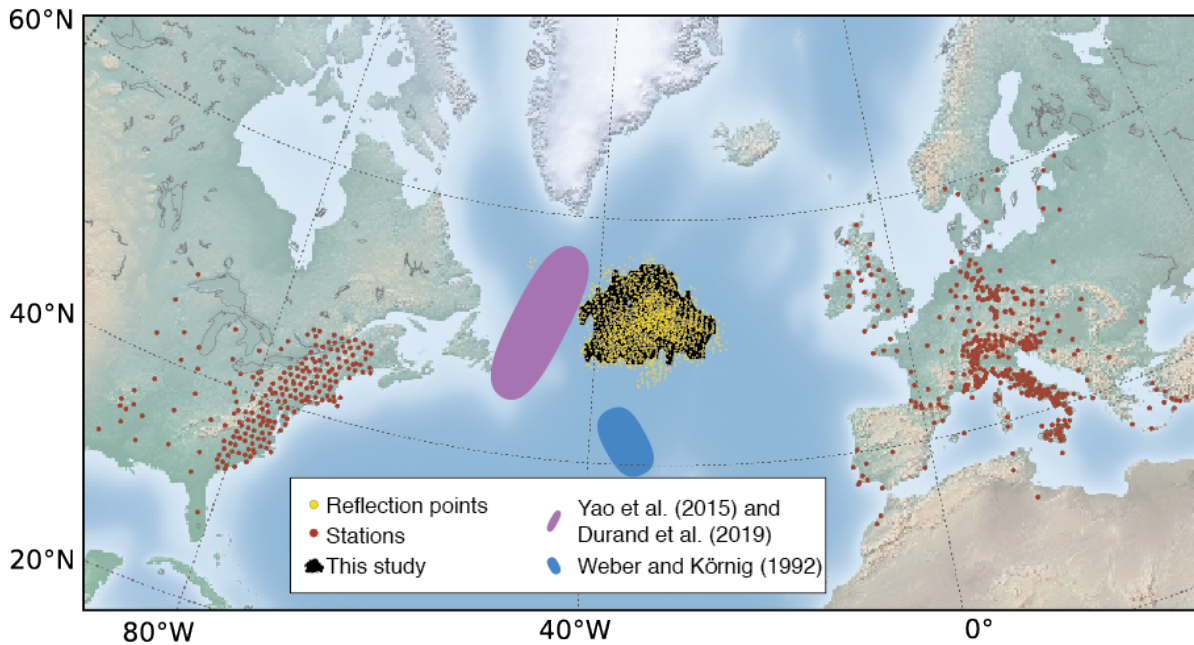


Figure 1: The red dots represent the ~900 stations in the US and Europe used for the study. The yellow dots represent the considered reflection points at the CMB and the black patch corresponds to the area covered by our final images. The closest previous studies are represented in blue (Weber and Körnig, 1992) and purple (Yao et al., 2015 and Durand et al., 2019).

2. Retrieving P-wave arrivals from noise correlations

Our dataset consists of 1 year (2014) of continuous seismic signals recorded by the vertical component of roughly 900 broadband stations in Europe and the US (Figure 1). The daily time series were downloaded from the Incorporated Research Institutions for Seismology (IRIS, <http://www.iris.edu/mda>) and European Integrated Data Archive (EIDA, <http://www.orfeus-eu.org/eida/eida.html>) data services. Details about the downloading and networks can be found in the supplementary materials S1 and Retailleau et al. (2017).

The correlation functions are computed between each station in the United States and each station in Europe, provided the stations were operating simultaneously for at least 100 days. The correlations are evaluated on 4-hour segments, frequency normalized, for all segments that do not contain strong earthquake signals. All correlations for a given station pair are then stacked over the entire year to optimize the convergence of the correlation function toward the Earth impulse response. The resulting correlation functions are filtered between 3 and 8 seconds of period, that is in the secondary microseism period band. Figures 2a and b show all these correlations as a function of inter-station distance and lag-time (the number of correlations stacked at all distances can be found in Figure S2). The two panels correspond to waves traveling from the US to Europe (Figure 2a, anticausal part of the correlations) and the opposite direction (Figure 2b, causal part). Teleseismic P and PcP arrivals are clearly visible for both directions and agree very well with the arrivals predicted using the TauP toolkit (Crotwell et al., 1999) using the IASP91 model (Kennett and Engdahl, 1991). No significant other arrivals are visible on Figure 2a and b leading to two options for a potential D" discontinuity: (1) No such discontinuity exists in this area or (2) the 3D structure is sufficiently complex to stack destructively in these averaged sections. Previous studies support the second option.

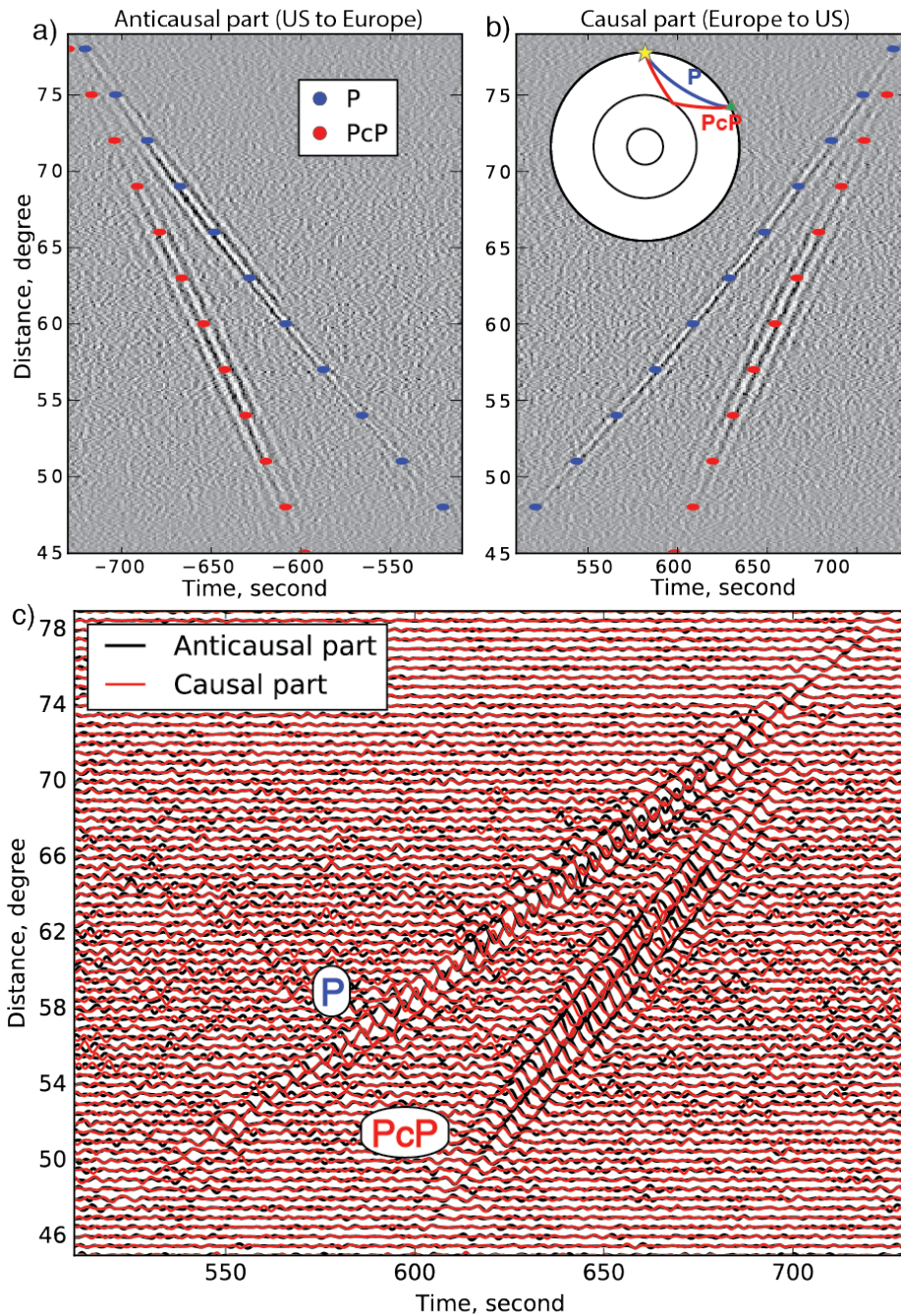


Figure 2: (a) Anticausal and (b) causal part of the correlation functions computed between US and European stations in the arrival time window of the P-waves. Signals are filtered from 3 to 8s. The correlations are stacked in 0.1 degrees distance bins. The blue and red dots represent P and PcP theoretical arrival times. (c) Direct comparison of the causal and anticausal part of the correlations stacked in 0.5 degrees distance bins.

A significant point is the apparent symmetry of the correlations, at least on average, observed for this P-wave propagation. We represent both the causal and the anticausal parts of the correlations in Figure 2c for a direct observation. While a good symmetry of the correlations is not necessary, it is a meaningful argument to support the sufficient convergence of the correlation toward the Green function in this frequency band. In other words, a similar bias that would be observed in both directions is very unlikely. Figure 3 shows the PcP source regions (Fresnel or stationary zones, e.g. Snieder, 2004) that match the stationary phase condition for the interference between PcPPcP and PcP at 7s of period. The two Fresnel zones correspond to the two propagation directions between a station in the US and a station in Europe. These two source areas are clearly distinct and it can therefore be said that anticausal and causal signals do not share the same microseism origin. We can also note that both areas are large compared to our study area. This implies that different locations in our study area are illuminated by very similar source areas (for causal and anticausal signals respectively), making it possible to confidently interpret relative variations of amplitude in our results. This phase combination (PcPPcP and PcP) is one of the possibilities to extract the PcP phase. For instance, a combination between a PKPPcP and a PKP phase is another possibility. Isolated energetic noise sources do not seem to play an important role over the entire year; no spurious phase is visible on this average section near the P-wave arrival (Li et al., 2020). We speculate that noise sources are sufficiently well distributed during the year and that scattering is strong enough at this period band to randomize the wavefield leading to relatively unbiased correlation functions. While this result is very promising we still choose to be careful with our interpretations and prioritize robustness.

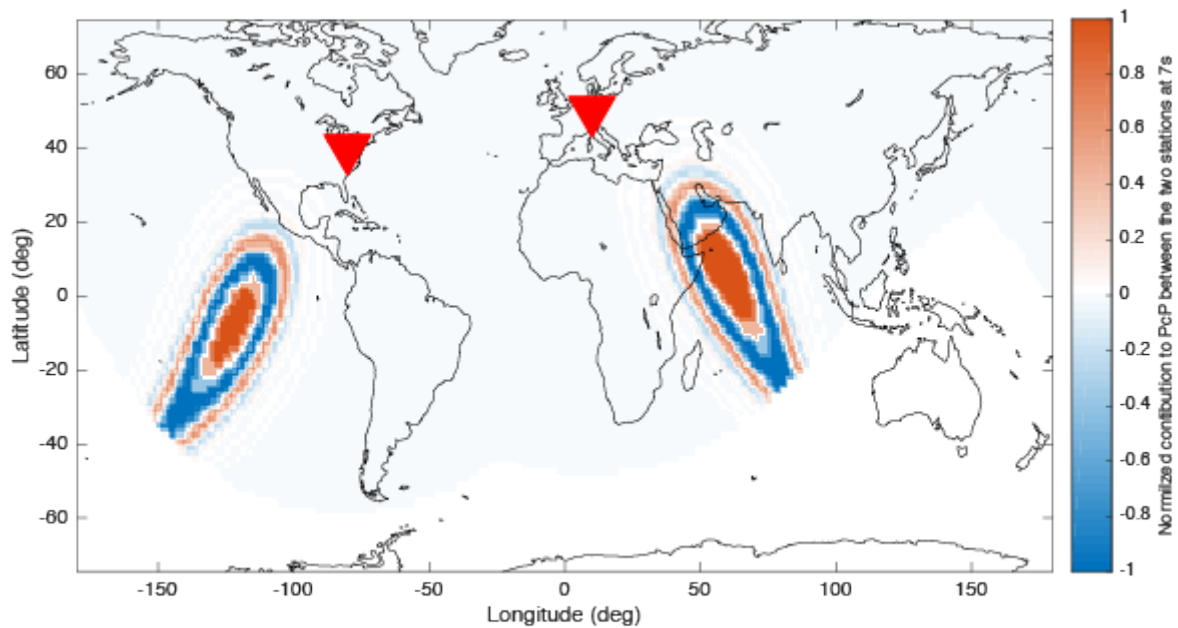


Figure 3: PcP phase source regions (Fresnel zones) that match the stationary phase condition for the interference between PcPPcP and PcP at 7s of period. The two lobes correspond to the source regions for both propagation directions. The two red triangles represent the two arrays used in this study. .

3. Mapping the reflectivity of the lowermost mantle

Figure 2a and b show spatially averaged signals meaning that sharp lateral variations naturally cancel out over the whole region. However, our dataset is sufficiently large to extract regional variations of reflectivity in the area highlighted by yellow dots in Figure 1. Our objective is to map the contribution of arrivals precursory to the PcP and thus potential reflection above the CMB. We describe here the main steps of the method; more details can be found in Supplementary material S1. To verify that our workflow does not include any bias and correct from the amplitude variations with geometrical and propagation effects, we apply the same process to synthetics computed in the 1D ak135 model with attenuation (ak135 of Kennett et al., 1995; synthetics from IRIS DMC, 2015; van Driel et al., 2015; Krischer et al., 2017). We generate the signals from a vertical force source located at each station location in Europe and recorded at all the US stations. We thus reproduce the propagation estimated by the correlation process applied on the real data. Because our correlations signals are fairly

symmetric, we stack them to produce a single image, but the following workflow is also applied on both the causal and anticausal parts of the correlations to get independent images. As compared to earthquake-based signals, a noise correlation technique that turns any seismic station into a virtual source allows the use of array processing on both the (virtual-) source and receiver side. This is particularly important to overcome low SNR of single station-to-station detections. At that scale, and with similar targets, this so-called double-beam analysis was first applied using nuclear explosion test sites as the source array (Kruger et al., 1993; Scherbaum et al., 1997), and then it proved its usefulness in the noise-imaging framework (Boué et al., 2014b).

Our workflow, applied on the data and on the synthetics, can be decomposed as follows (a detailed diagram is available in the supplementary material, Figure S1):

(1) Constitution of subarrays in both the US and Europe by selecting, on each point of a grid of spacing 110 km x 140 km, all stations within a 150 km radius. Subarrays are then paired with all subarrays from the other continent. The corresponding reflection points below the Atlantic Ocean are represented with yellow dots in Figure 1.

(2) Computation of double-beam transforms (time-slowness analysis, Rost and Thomas, 2002; Boué et al., 2014b) using each combination of sub-arrays provided they contain at least 200 pairs of stations (i.e correlation functions). Figure 4a shows a vespagram (time-slowness representation) obtained for a single combination of subarrays. For sake of simplicity, we here consider that the slowness is the same at both subarrays for a given phase.

(3) Construction of time and slowness values pairs of potential reflection points below the lowest point of the P-direct wave are computed using the TauPtoolkit (Crotwell et al., 1999) for a propagation in a 1D model ak135 (Kennett and Engdahl, 1991). These hypothetical reflection points, each corresponding to a given depth, are represented on top of the vespagram in Figure 4a as green dots. The amplitude of the beam is extracted at each depth as shown in Figure 4b. We name R_z this depth dependent reflectivity function derived from our beamforming analysis. This figure shows the PcP phase at the correct depth (~2890 km, corresponding to

the CMB) along with a precursory arrival labeled as P*P. We name I_z the function of depth z obtained through the same process using synthetic waveforms computed in ak135. The generalization of this analysis to all subarray combinations (each of which consists of at least 200 stations) is presented in Figure 4c. Each R_z reflectivity function, extracted from each array pair, is represented as a function of the inter-array distance along the great circle. The first signal, at the beginning of each curve, corresponds to the P arrival. The associated depth varies with the turning point of the phase, thus with the inter-array distance.

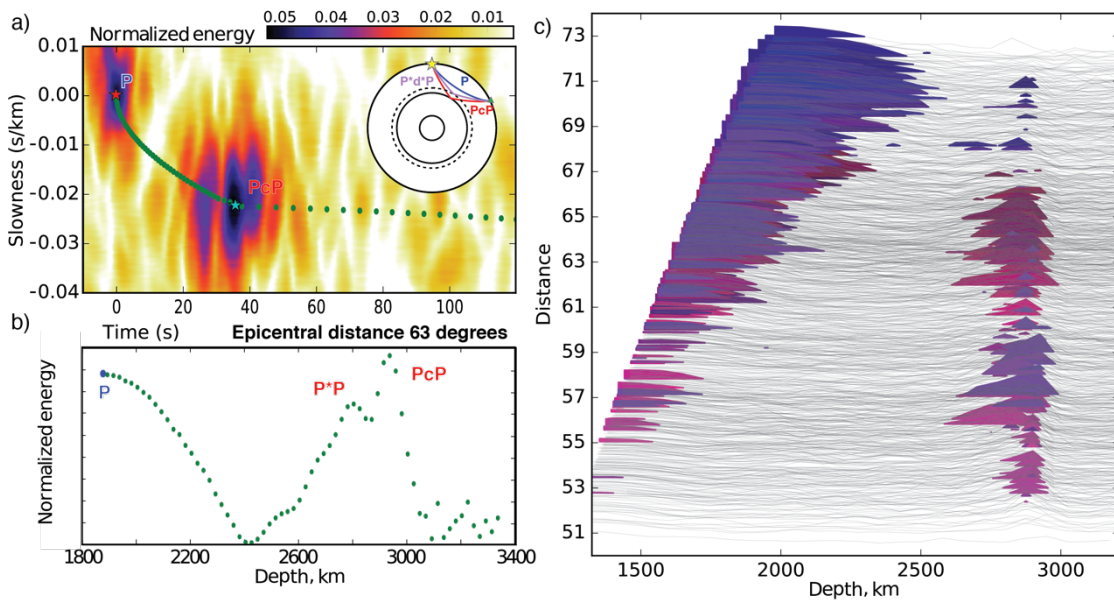


Figure 4: (a) Example of a vespagram from a single subarray combination (of an epicentral distance of 63 degrees). The stars correspond to the P and PcP arrivals. (b) Normalized R_z function extracted from (a). (c) R_z functions for all subarray combinations as a function of inter-array distance. Purple color highlights P and PcP signals.

The second signal, at about 2890 km depth, corresponds to the detection of the CMB. This signal is obtained with most subarray combinations. This first-order observation confirms that we can extract large-scale structural information even using a subset of correlation signals. Figure 4c also reveals that this signal is not depicting a laterally homogeneous interface; indeed very little signal is observable at the CMB at some distances, and some precursory reflected phases appear at about 2600 km. Absolute amplitudes are difficult to assess using correlation functions and would require a better understanding of the noise sources to be

unambiguously interpreted. Nevertheless, we note that for a given pair of stations the same noise sources are illuminating both the CMB and potential shallower reflectors. It is therefore justified to discuss the relative amplitude of the reflected phases with respect to the reflection at the CMB. As mentioned earlier in the paper (Figure 3), one can also notice that the size of our target is smaller than the noise source Fresnel zone of the PcP signals by a factor 4. This suggests that the local comparison between the subarrays is also justified.

To build the reflection maps, we first normalize each reflectivity function R_z by the average amplitude $\langle R_{2890} \rangle$ at the CMB (2890 km of depth) with $\langle . \rangle$ denoting the average over all paths, and we proceed identically with the synthetics analysis by dividing each function I_z by $\langle I_{2890} \rangle$. We then divide each function R_z and I_z by the amplitude I_{2890} of the corresponding path at the CMB to correct the amplitude variations due to geometrical spreading and attenuation. The final R_z and I_z functions can be seen as a proxy of the P wave reflectivity relative to the CMB discontinuity. After this normalization, the theoretical CMB within I_z functions should show up with a value of 1.

Most studies that look for lower mantle heterogeneities use shear waves propagating between about 70 to 85 degrees of epicentral distances. In this distance range, precursory arrivals are usually well separated from S and ScS branches (about 10s separation, e.g. Kito et al. 2007, Lay and Garnero 2011). In our case, using the P waves emerging alone from correlations (no S waves) we work between 51 and 73 degrees. For the largest distance, we expect to have less than a dominant period lag between PcP and potential precursory arrival (Figure S3). To verify the geographical distribution of the heterogeneities as seen in Figure 4c (as a function of distance) functions R_z (and similarly I_z) are projected on a latitude-longitude 950 km x 1250 km (680 km x 520 km at the CMB) grid to form a 3D final image. We sample the grid by a longitude and latitude spacing of 0.5 degrees. At each point of the grid we average the functions R_z reflected at the location provided there are at least four R_z functions (i.e. array combinations). Figure 5b shows the interpolated values R_z at six different depths from 2470

km in the mantle to 3170 km in the outer core. The same process is performed from the synthetic functions I_z whose results are shown in Figure 5a as a reference. This reference Figure shows that our processing does not introduce lateral bias and is calibrated to resolve the CMB. We perform a bootstrap analysis to assess the quality of the 3D image we reconstruct (Supplementary Figure S4). We perform 1000 random samplings of 75% of the subarray combinations. Figure S4a and b represent the average value and standard deviation obtained between all tests at the different locations can. The averaged 3D image (Figure S4a) is very consistent with the overall result in Figure 5b. The low value of the standard deviation, that is to say various combinations of arrays give similar estimations for the same reflector point, is a good indication that our results are robust; small scale heterogeneities of the mantle are not dominating the image.

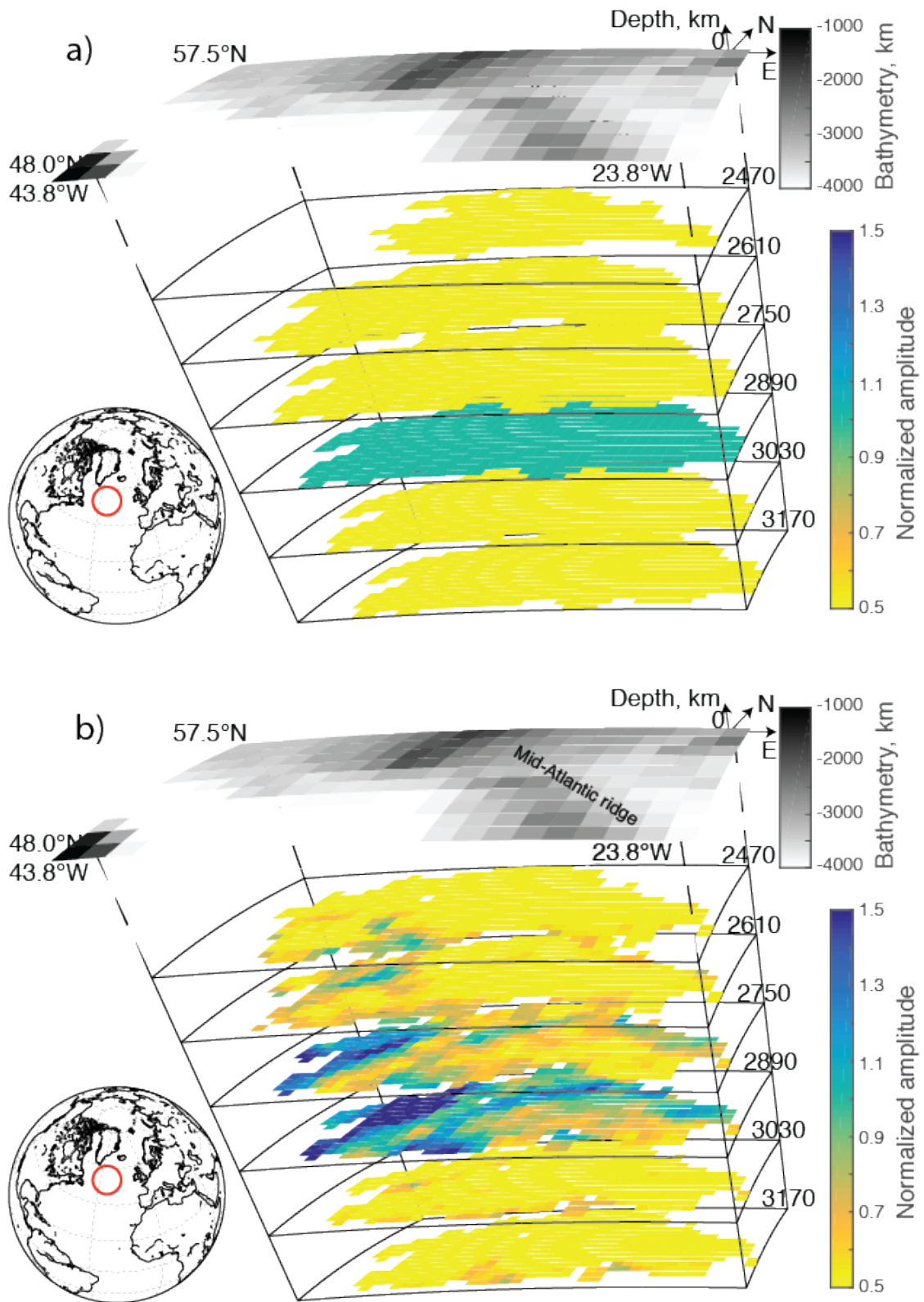


Figure 5: Pseudo reflectivity 3D image obtained from (a) synthetic waveforms (ak135) and (b) signals extracted from ambient noise records. CMB is visible at 2890 km depth.

4. Discussion

As expected, the result obtained from synthetics generated using a 1D model, in Figure 5a, shows a laterally homogeneous reflection at the CMB (with a value of 1 due to our normalization) and no reflection above or beneath. This shows that our array processing and overall imaging workflow does not introduce artifacts. The result obtained with noise-based data, in Figure 5b, also shows a major reflection at the CMB but with strong lateral variations and reflected energy at smaller depths. This coincides with the observations made in Figure 4c. At depth of the CMB, R_{2890} shows a clear high reflectivity anomaly (blue area) of about 200 km x 100 km in the North West region. Since the amplitudes are normalized so that the average amplitude at the CMB is set to one, this observed high amplitude anomaly implies a strong reflectivity increase relative to theoretical CMB. This structure extends upward in the lower mantle to 2600 km depth. We can also note that, as was seen in Figure 4c, there is no energy reflected in the outer core, except from the amplitude introduced by finite frequency effect of the PcP pulse width that is centered at the CMB depth (this effect already vanished on the first slice below the CMB at 3030 km depth). One could question if the precursory signals could be an effect of broadening of the PcP pulse. We expect a broadening effect of stacking to affect depths above and below the CMB after migration. We notice in Figure 4c that the wiggles detected prior to the PcP have a much larger amplitude than the small amplitude oscillations visible below the CMB. The comparison with ak135 synthetics confirms that clear reflected waves originate from above the CMB.

The process we use to detect arrivals around the CMB combines the envelope vespagrams generated at the multiple reflection points. While this process makes the observations more robust, the stack smooths lateral variations. As mentioned earlier, we do not expect to recover absolute amplitudes with ambient noise correlations and we aim at detecting the precursory arrivals and to compare their relative amplitude with PcP. The CMB amplitude is also normalized by its average value, meaning that a value of 1 corresponds to the expected CMB contrast (defined by ak135). The observed structure, which extends upward to 2600 km, is too

thick for a ULVZ, however, it is consistent in terms of size with other D'' observations in other regions (Lay, 2015, Li et al., 2019). In contrast, the South East region of the image shows a lower reflectivity at the CMB. The transition between these two areas reveals complex patterns with a typical size of about 50 km. Fluctuations of the amplitude at the CMB range from 0.5 to 1.5. We will interpret these variations of about 50% of the reflectivity cautiously due to the difficulty to properly calibrate correlation amplitudes (as explained above) and also due to the possible impact of a critical reflection as discussed later. However, we show a raw image without further processing to highlight the spatial variability of the structures. Indeed, the characteristic size of the heterogeneities we see on Figure 5b are in good agreement with previous observations in neighboring areas of roughly 300 km thick and laterally discontinuous D'' reflectors (Yao et al., 2015, Durand et al., 2019). A full comparison would probably require combining earthquake and microseism data as well as the S waves extracted from microseism excitation correlations. Such microseism based S wave signals have been proved to exist for very energetic oceanic events (Nishida and Takagi, 2016), but appear to be more difficult to extract than P-waves

To verify that our results are not significantly impacted by noise source distribution or transient signals, we compare the images produced by the anticausal and causal part of the correlation separately (i.e waves traveling from the US to Europe and in the reverse direction). The results are presented in Figure S5. The large-scale variations as discussed above are visible with a positive anomaly in the North West area in both cases. These images also help to estimate a lateral resolution at the CMB for Figure 5 of roughly 100 km. Indeed, at lower scales there are some differences between the results obtained with the causal and the anticausal part of the correlations. We represent the difference between the results obtained with the causal and anticausal parts of the correlations in Figure S6. Other parameters such as the inter-subarray distance or the number of stacked signals per bin to construct the image are also possible sources of artefacts and biases in our final result. To check that there is no such bias from these parameters we compared them to the image at the CMB (see Figure S7). No significant

bias emerges from these comparisons. For instance, isovalues of the mean inter-subarray distance are crossing the main features of the image. Finally, the bootstrap analysis (Figure S4) shows that no subarray pair dominates the results and creates unreliable observations.

Until now, we only used the envelope of the vespagrams for our analyses. We also perform the same process while keeping track of the phase information, meaning not computing the envelope, to analyze the relative polarity of the precursory arrivals. Figure 6b shows these observations of R_z/R_{2980} averaged over two different areas (zone A and zone B) and for both the data and the synthetic waveforms. As already discussed, the limited bandwidth of the secondary microseism limits the temporal resolution of the pulses we extract resulting in a possible overlap of the CMB arrival with the precursory signal. It is thus not straightforward to conclude on the phase of precursors. There does not seem to be a polarity flip, but we cannot conclude about a potential phase shift to better constrain the real reflection coefficient. Looking at the averaged pulse observed for the positive anomaly in the North West area (zone A, red rectangle in Figure 6) it seems that precursory arrival amplitude is high when the CMB reflection is also high. In terms of reflection coefficients, this coincides with a high-velocity D" layer for both P and S waves (as it will be developed later). Looking now at the pulse observed for the other region, which shows a lower reflectivity at the CMB (zone B, black rectangle, Figure 6a), the existence of a precursory signal is less evident. It is interesting to note that the synthetic signals, for which the same processing workflow was applied, show in addition to a clear CMB reflection a small precursory signal at 2 750 km depth, where ak135 experiences a velocity gradient decrease. Our simple migration scheme allows us to properly capture this anomaly. Finally, both data-based averaged pulses (Figure 6b) show an asymmetric pattern with apparent lower frequencies above the CMB compared to below it. This is mostly due to a stretching effect introduced by the depth migration of the correlation functions (see green dots on Figure 4a). This effect appears on the synthetic pulses shown on Figure 6b, but it is particularly clear if we take a single signal (Figure 7g).

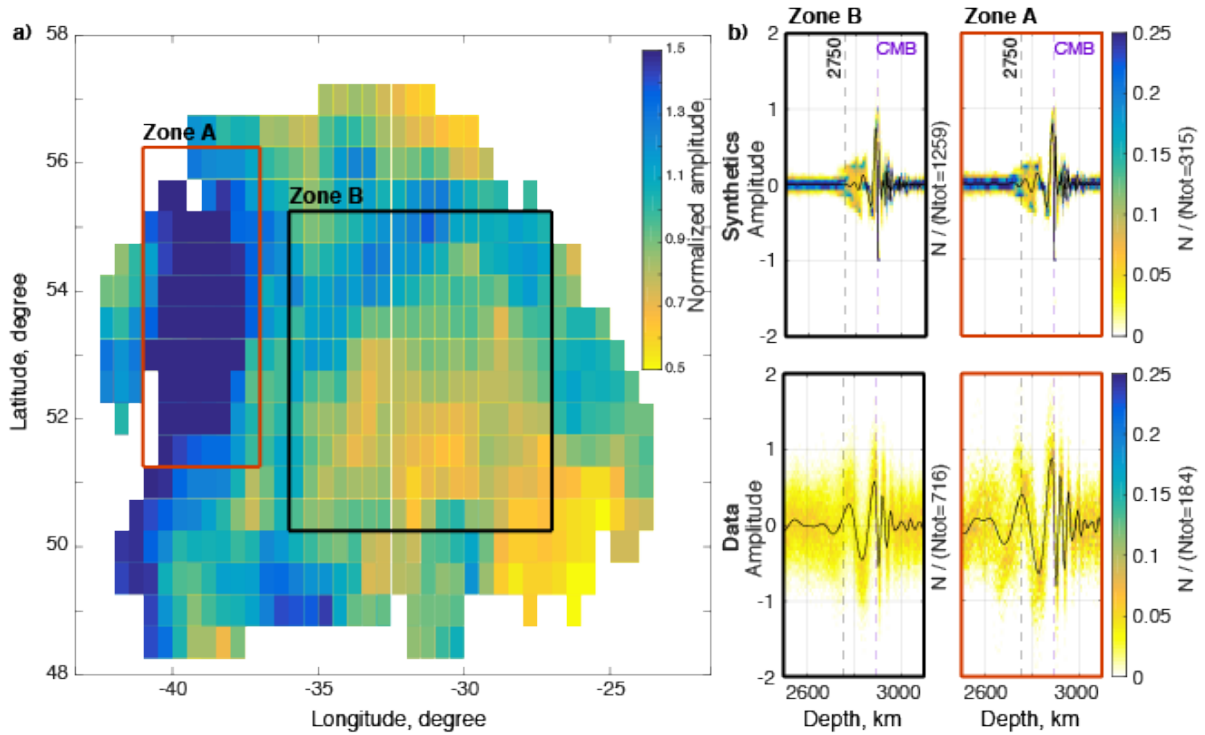


Figure 6: (a) Pseudo reflectivity at the depth of CMB as seen in Figure 5b. The two boxes show areas where signals are extracted for polarity analysis, a zone with positive anomaly and an average zone in red and black respectively. (b) Density representation of all phase-preserved regionalized I_z functions for the synthetics (top) and phase-preserved regionalized R_z functions from data (bottom) for the two areas.

To go deeper in our interpretation of the precursory signals we are observing, we now consider very simple 1D models of positive P-wave velocity increase in the last kilometers of the lower mantle. Starting from ak135 as a reference (in black, Figure 7), we consider 4 different perturbed models to describe a hypothetical D'' layer (Figure 7a): two models with a simple positive step discontinuity 250 km above the CMB, and two models with a smoother gradient starting around 300 km above the CMB. In both cases a P-wave velocity perturbation (δV_p), is fixed to 2% and 4% respectively ($\delta V_s=0$), relative to ak135 within the entire D'' layer. We then recreate the configuration of one set of subarrays, with a source on one side of the ocean and 249 stations on the other side (assimilating the virtual station on one side of the ocean and all the others on the other side). The average distance is 62 degrees. Synthetic signals

are generated using *axisem* (Nissen-Meyer et al., 2014) for a vertical point force source at the surface. The signals are filtered in the 3-8 sec period band, similarly to the data. We compute the vespagram for each model following the process used to generate Figure 4a, without taking the envelope (Figure 7b-f). We extract each function I_z from the vespagrams, using the migration described in Figure 4. We represent the different I_z functions in Figure 7g (the colors follow Figure 7a). Figure 7g is comparable to Figure 6b but for a single reflection point (no spatial averaging). Indeed, in this new and simpler case, the stretching effect due to the migration is clearly visible.

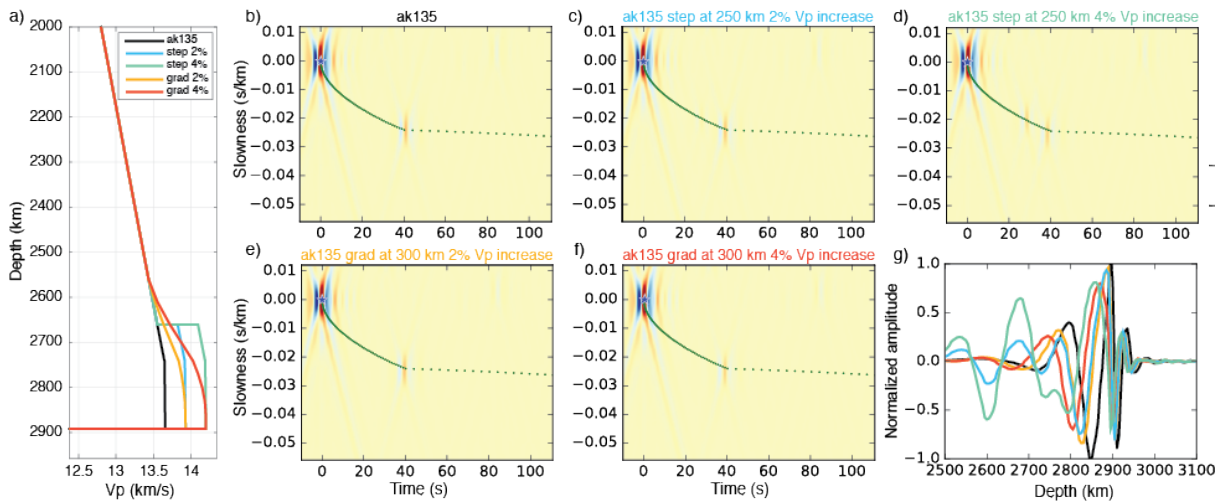


Figure 7: (a) proposed velocity models. (b-f) Vespagrams computed for each model at a distance of 62° . (g) I_z functions obtained following the same process as in Figure 6b and for each model.

Both step models generate a clear precursory signal centered around 2650 km and visible on Figure 7g. We can observe a tenuous PdP arrival in Figure 7d, but similar observation is difficult for a 2% step increase (Figure 7c). The signal of the 4% step increase visible on Figure 7g is the closest of our observation for zone A on Figure 6b (red rectangle). Both models with a smoother D" velocity increase (grad 2% and grad 4%) show a slight stretching toward lower depth (expected for a velocity increase) with no clear precursors. These simple examples show that, using our workflow, we can detect a 250 km thick D" and distinguish between sharp (step)

and smooth (gradient) velocity increase. By comparing Figure 7g with 6b, the strong reflectivity anomaly on the North West edge of our study area (visible on Figure 5 and discussed as zone A on Figure 6) would probably give a best fit with an intermediate model between step 4% and grad 4%. The absence of a clear precursory arrival on many of the signals from other regions of our study zone (Figure 4c) could indicate smoother velocity variation.

Based on theoretical reflection coefficients on both the CMB and on a hypothetical D" discontinuity, we can estimate the minimal requirements in terms of structural variation to explain our observations. First, theoretical reflection coefficients are computed for the CMB and a 250 km thick (step) D" for all combinations of parameters that define the anomaly, including δV_p , δV_s and $\delta \rho$ (density). These parameters are ranging from -20% to +20%. In order to match our signal processing workflow, all reflection coefficients are then normalized by a not-perturbed reference CMB reflectivity at each epicentral distance. The supplementary Figure S8 gives an example of representation for these 3D parametric normalized reflection coefficients. Figure 8 shows reflection coefficients as a function of incidence angles and epicentral distances (without normalization) for 5 models including ak135. By comparing normalized reflection coefficients to what we observe Figure 5b and for the high reflectivity anomaly (zone A, Figure 6a) with a high reflectivity above ($R_{2610}=1$) and at the CMB ($R_{2890}=1.2$) the smallest perturbation needed is about $\delta V_s=+8\%$ and $\delta V_p=+4\%$ if we consider a 250 km thick D" step perturbation of ak135 (similar to the Figure 7, and here named model step1). Using the same approach we can evaluate that a decrease of V_s of about $\delta V_s=-4\%$ within the last 250 km of the lower mantle (model step2) could explain zone B (Figure 6a) where we observe a low D" reflectivity ($R_{2610}=0.2$) and a low CMB reflectivity ($R_{2890}=0.8$). Figure 8 shows theoretical reflection coefficients for both step 1 and step 2. These two simple models correspond to a first-order evaluation that tends to show that Figure 5b contains structural information. However, we note that density is poorly constrained by this approach and can stay almost the same with less than a percent of variation. V_s perturbation is also not very well constrained especially for a positive V_p anomaly, which leads to a critical reflection at short

epicentral distances (see Figure 8 and S8). A higher sensitivity on V_p is not surprising since we are only dealing with P waves.

The velocity perturbations estimated here are a little high and difficult to explain in the framework of a perovskite / post-perovskite transition where we expect weak velocity perturbation for D" (Cobden et al. 2015). But two remarks can be made to support our observations. First, a P-wave velocity increase of about $\delta V_p=+4\%$ is in good agreement, although in the upper range, with previous seismological studies in neighboring regions (Weber and Körnig, 1992; Durand et al., 2019). A greater V_s discontinuity ($\delta V_s=+8\%$), on the other hand, farther away from previous observations (Yao et al., 2015; Durand et al., 2019), but again not well resolved in our case. For a fixed value of $\delta V_p=+4\%$, a positive jump of V_s has a relatively small influence on the observed P-wave reflectivity of the D" layer; the observed δV_s is in fact mostly controlled by the slight increase of the CMB reflectivity (see the difference between model step1 and step4 in Figure 8), which is less resolved due to PdP pulse broadening and possible overlapping with PcP. Second, the fact that we are observing what appears to be relatively strong velocity perturbations could be related to the presence of critical reflection at relatively short epicentral distances. The different models with a positive δV_p presented in Figure 8 (step1, step3 and step4) show sharp increases of reflectivity between 50° and 70° of epicentral distances (similar range that we are using in this study). By possibly mixing pre- and post-critical reflections during the required spatial averaging of the beamformed correlation functions (Figure 4c), we are aware that we may introduce non-physical reflectivity values in our result (Figure 5b). Even if the spatial averaging also helps us to smooth these possible biases, the quantification of the influence of such critical reflections would require an a priori knowledge of the D" structure and could be a subject of a separate study (with synthetic data). Finally, we speculate that the amount of data involved in our method might also be a very efficient way to precisely measure the critical angle for precursory reflections and thus give a very strong constraint on δV_p and thickness of the D", but this is beyond the scope of the present article, and will be addressed in future work.

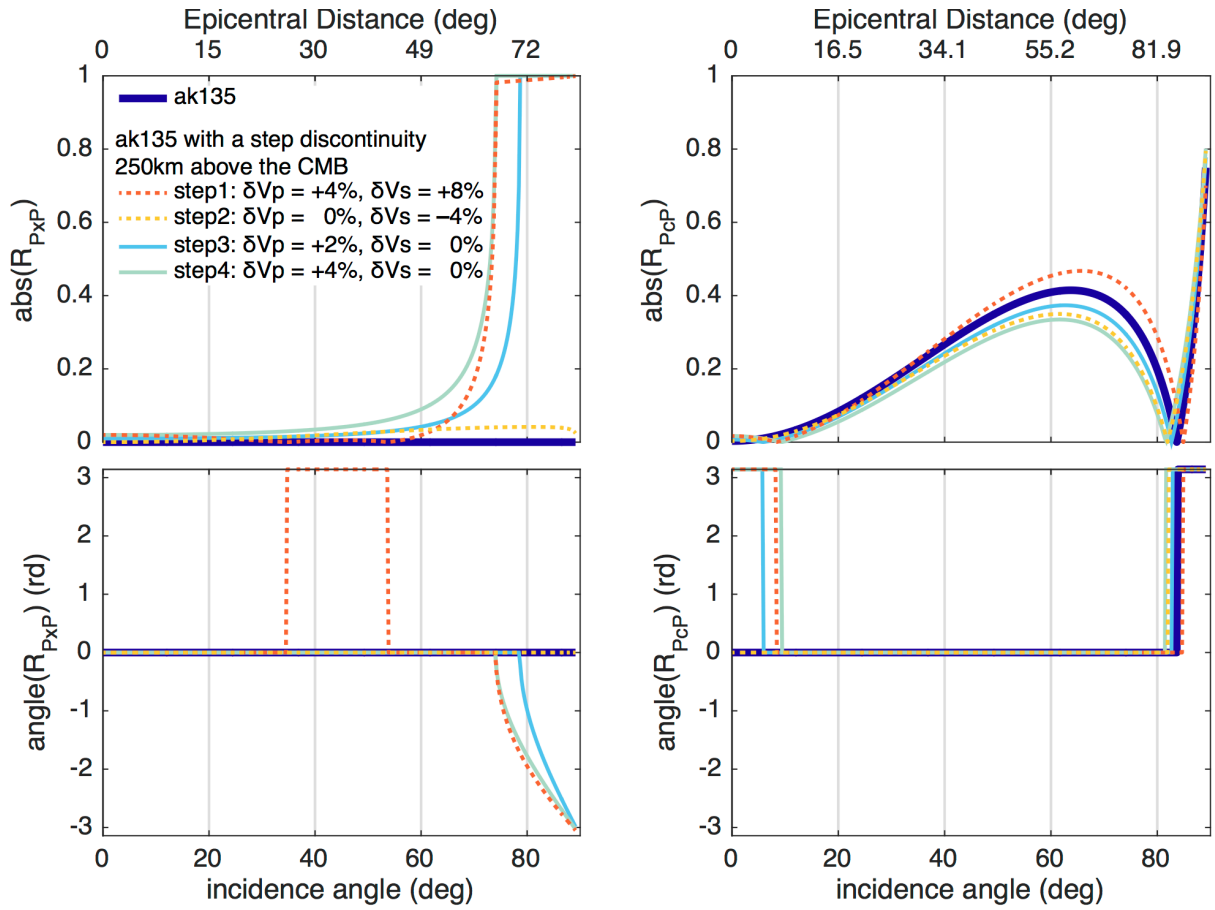


Figure 8: Reflection coefficient amplitude (top) and phase (bottom) at the CMB (right) and for a step-like D'' layer 250 km above the CMB (left) computed as a function of epicentral distances and for different models. Thick blue lines correspond to ak135. Dotted lines correspond to minimal requirements to explain red and black areas in Figure 6. Light blue and green lines correspond to the 2 step models discussed in Figure 7.

5. Conclusions

We have built a 3D image of the CMB region under the Atlantic Ocean from the correlations computed between one year records of seismic stations in Europe and in the US. Figure 5b constitutes a first tentative, 3D image of the CMB region derived from microseism excitation. Even if critical reflection may introduce a bias of amplitude in the image, we are confident in the shape and spatial extension of our detection. We compared our observations to different possible models containing a hypothetical D" layer. A model containing a Vp velocity increase of 4% is consistent with our observations and neighboring studies.

Earthquake data and careful synthetic tests would help to better constrain the structural properties. Our methodology would also greatly benefit from other observations such as secondary microseism S-wave reconstruction (Nishida and Takagi, 2016) and/or high-frequency signals from specific storms (for example typhoon Ioke, Retailleau and Gualtieri, 2019).

The lowermost mantle is known to incorporate multi-scale heterogeneities with direct consequences for both mantle and core dynamics (Tkalčić et al., 2015). Detailed studies of high frequency scattered waves and lower frequency waves used for global tomography already give a good picture of these heterogeneities where earthquake data are available. We believe that the present approach can help link up these different scales to form a more comprehensive image of the lowermost mantle by providing complementary information where earthquake data are scarce.

Appendix

European data		
Network	N stations	Data center
BW	1	LMU, Germany (<i>Geophysical Observatory, University of Munchen</i> [2001])
CH	33	ETH, Switzerland (<i>Swiss Seismological Service (SED) at ETH Zurich</i> [1983])
CR	1	ODC, Netherlands
CZ	13	CAS (<i>Institute of Geophysics, Academy of Sciences of the Czech Republic</i> [1973])
FR	33	RESIF, France (<i>RESIF</i> [1995])
G	3	GEOSCOPE, France (<i>IPGP and EOST</i> [1982])
GE	16	GFZ, Germany (<i>GEOFON Data Centre</i> [1993])
GR	43	BGR, Germany
IV	139	INGV, Italy
MN	17	INGV, Italy
NL	1	ODC, Netherlands
OE	11	Austrian Seismic network (ZAMG Central Institute for Meteorology and Geodynamics)
SI	6	INGV, Italy
SL	22	SEA, Slovenia (<i>Slovenian Environment Agency</i> [2001])
SX	11	SXNET Saxon Seismic Network (University of Leipzig, Germany)
TH	16	Thüringer Seismisches Netz, Germany (Friedrich-Schiller-Universitaet Jena)

Table A1. The seismological networks used in Europe. N is the number of stations

United States data		
Network	N stations	Data center
IU	6	Global Seismograph Network (GSN-IRIS/USGS) (<i>Albuquerque Seismological Laboratory (ASL)/USGS</i> [1988])
LD	1	Lamont-Doherty cooperative Seismographic network (Columbia University)
TA	177	USArray Transportable Array (<i>IRIS Transportable Array</i> [2003])
US	23	United States National Seismic Network (<i>Albuquerque Seismological Laboratory (ASL)/USGS</i> [1990])

Table A2. The seismological networks used in the US. N is the number of stations.

Acknowledgments

The dataset was downloaded and processed using python and the seismological community scientific library **obspy** (Krischer et al., 2015). The figures were produced using Python and MATLAB and the Python module **basemap** was used to produce the map. The facilities of IRIS Data Services, and specifically the IRIS Data Management Center, were used to access the waveforms, related metadata, and/or derived products used in this study (<http://www.iris.edu/mda>). The IRIS Data Services are funded through the Seismological Facilities for the Advancement of Geoscience and EarthScope (SAGE) Proposal of the National Science Foundation under Cooperative Agreement EAR-1261681.

The computation of the correlation functions presented in this paper was performed performed using the GRICAD infrastructure (<https://gricad.univ-grenoble-alpes.fr>), which is partly supported by the Equip@Meso project (reference ANR-10-EQPX-29-01) of the programme Investissements d'Avenir supervised by the Agence Nationale pour la Recherche. This work has been supported by a grant from Labex OSUG@2020 (Investissements d'avenir – ANR10 LABX56) and Fondation Simone et Cino Del Duca, Institut de France (Prix scientifique 2013). We acknowledge the support from the European Research Council (ERC) under the European Union's Horizon 2020 research and innovation program (grant agreement No 742335, F-IMAGE). The research of LR was supported by Pacific Gas and Electric. We thank K. Schaukowitch and the Hume center for writing and speaking at Stanford for useful comments that helped us to improve the manuscript. We thank the Editor, Michael Ritzwoller, Stéphanie Durand and two anonymous reviewers for their comments and suggestions which helped to improve the quality of this article.

References

1. Ardhuin, F., Stutzmann, E., Schimmel, M., & Mangeney, A. (2011). Ocean wave sources of seismic noise. *Journal of Geophysical Research: Oceans*, 116(C9).
2. Boué, P., Poli, P., Campillo, M., Pedersen, H., Briand, X., & Roux, P. (2013). Teleseismic correlations of ambient seismic noise for deep global imaging of the Earth. *Geophysical Journal International*, 194(2), 844-848.
3. Boué, P., Poli, P., Campillo, M., & Roux, P. (2014). Reverberations, coda waves and ambient noise: Correlations at the global scale and retrieval of the deep phases. *Earth and Planetary Science Letters*, 391, 137-145.
4. Boué, P., Roux, P., Campillo, M., & Briand, X. (2014). Phase velocity tomography of surface waves using ambient noise cross correlation and array processing. *Journal of Geophysical Research: Solid Earth*, 119(1), 519-529.
5. Boyet, M., & Carlson, R. W. (2005). ¹⁴²Nd evidence for early (> 4.53 Ga) global differentiation of the silicate Earth. *Science*, 309(5734), 576-581.
6. Bullen, K. E. (1949). Compressibility-pressure hypothesis and the Earth's interior. *Geophysical Journal International*, 5, 335-368.
7. Cobden, L., Thomas, C., & Trampert, J. (2015). Seismic detection of post-perovskite inside the Earth. In *The Earth's Heterogeneous Mantle* (pp. 391-440). Springer, Cham.
8. Crotwell, H. P., Owens, T. J., & Ritsema, J. (1999). The TauP Toolkit: Flexible seismic travel-time and ray-path utilities. *Seismological Research Letters*, 70, 154-160.

9. Department of Earth and Environmental Sciences, Geophysical Observatory, University of Munchen (2001). BayernNetz. International Federation of Digital Seismograph Networks. Other Seismic Network. <https://doi.org/10.7914/SN/BW10.7914/SN/BW>
10. van Driel, M., Krischer, L., Stähler, S. C., Hosseini, K., and Nissen-Meyer, T.: Instaseis: instant global seismograms based on a broadband waveform database, *Solid Earth*, 6, 701-717, <https://doi.org/10.5194/se-6-701-2015>, 2015.
11. Durand, S., Debayle, E., Ricard, Y., & Lambotte, S. (2016). Seismic evidence for a change in the large-scale tomographic pattern across the D'' layer. *Geophysical Research Letters*, 43(15), 7928-7936.
12. Durand, S., Debayle, E., Ricard, Y., Zaroli, C., & Lambotte, S. (2017). Confirmation of a change in the global shear velocity pattern at around 1000 km depth. *Geophysical Journal International*, 211(3), 1628-1639.
13. S. Durand, C. Thomas, J.M. Jackson (2019) Constraints on D'' beneath the North Atlantic region from P and S traveltimes and amplitudes, *Geophysical Journal International* 216 (2), 1132-1144.
14. Dziewonski, A. M., & Anderson, D. L. (1981). Preliminary reference Earth model. *Physics of the earth and planetary interiors*, 25(4), 297-356.
15. Earle, P. S., & Shearer, P. M. (1997). Observations of PKKP precursors used to estimate small-scale topography on the core-mantle boundary. *Science*, 277(5326), 667-670.

16. Fichtner, A., Stehly, L., Ermert, L., & Boehm, C. (2016). Generalised interferometry-I. Theory for inter-station correlations. *Geophysical Journal International*, ggw420.
17. French, S. W., & Romanowicz, B. (2015). Broad plumes rooted at the base of the Earth's mantle beneath major hotspots. *Nature*, 525(7567), 95.
18. Garnero, E. J. (2000). Lower mantle heterogeneity. *Annu. Rev. Earth Planet. Sci*, 28, 509-537.
19. Garnero, E. J., McNamara, A. K., & Shim, S. H. (2016). Continent-sized anomalous zones with low seismic velocity at the base of Earth's mantle. *Nature Geoscience*, 9(7), 481.
20. Gassner, A., Thomas, C., Krüger, F., & Weber, M. (2015). Probing the core–mantle boundary beneath Europe and Western Eurasia: A detailed study using PcP. *Physics of the Earth and Planetary Interiors*, 246, 9-24.
21. GEOFON Data Centre (1993), Geofon seismic network, deutsches geoforschungszentrum GFZ, doi: 10.14470/TR560404, other/Seismic Network.
22. GEOSCOPE - French Global Network of broadband seismic stations. Institut de Physique du Globe de Paris & Ecole et Observatoire des Sciences de la Terre de Strasbourg (EOST) - doi:10.18715/GEOSCOPE.G
23. Gerstoft, P., Shearer, P.M., Harmon, N. & Zhang, J., 2008. Global P, PP, and PKP wave microseisms observed from distant storms, *Geophys. Res. Lett.*, **35**, L23306, doi:10.1029/2008GL036111.

24. Glatzmaier, G.A., Coe, R.S., Hongre., L. & Roberts, P.H., 1999. The role of the Earth's mantle in controlling the frequency of geomagnetic reversals, *Nature*, 401, 885–890
25. Hasselmann, K. (1963). A statistical analysis of the generation of microseisms. *Reviews of Geophysics*, 1(2), 177-210.
26. Hernlund, J. & McNamara, A.K., 2015. The core-mantle boundary region, in *Treatise on Geophysics*, 2nd edn, Vol. 7, pp. 461–519, Elsevier.
27. Hillers, G., Graham, N., Campillo, M., Kedar, S., Landès, M., & Shapiro, N. (2012). Global oceanic microseism sources as seen by seismic arrays and predicted by wave action models. *Geochemistry, Geophysics, Geosystems*, 13(1).
28. Houser, C., Masters, G., Shearer, P., & Laske, G. (2008). Shear and compressional velocity models of the mantle from cluster analysis of long-period waveforms. *Geophysical Journal International*, 174(1), 195-212.
29. Huang, H. H., Lin, F. C., Tsai, V. C., & Koper, K. D. (2015). High-resolution probing of inner core structure with seismic interferometry. *Geophysical Research Letters*, 42(24), 10-622.
30. Institute of Geophysics, Academy of Sciences of the Czech Republic (1973), Czech regional seismic network, international federation of digital seismograph networks, doi:10.7914/SN/CZ, other/Seismic Network.
31. IRIS DMC (2015), Data Services Products: Synthetics Engine, <https://doi.org/10.17611/DP/SYNGINE.1>.

32. Kedar, S., Longuet-Higgins, M., Webb, F., Graham, N., Clayton, R., & Jones, C. (2008). The origin of deep ocean microseisms in the North Atlantic Ocean: The Royal Society. *Proceedings of the Royal Society of London A: Mathematical, Physical and Engineering Sciences*, 464(2091), 777–793.
33. Kennett, B. L. N., & Engdahl, E. R. (1991). Traveltimes for global earthquake location and phase identification. *Geophysical Journal International*, 105(2), 429-465.
34. Kennett, B. L. N., Engdahl, E. R., & Buland, R. (1995). Constraints on seismic velocities in the Earth from traveltimes. *Geophysical Journal International*, 122(1), 108-124.
35. Kennett, B. L. N., & Pham, T. S. (2018). The nature of Earth's correlation wavefield: late coda of large earthquakes. *Proc. R. Soc. A*, 474(2214), 20180082.
36. Kito, T., Rost, S., Thomas, C., & Garnero, E. J. (2007). New insights into the P-and S-wave velocity structure of the D "discontinuity beneath the Cocos plate. *Geophysical Journal International*, 169(2), 631-645.
37. Koelemeijer, P., Ritsema, J., Deuss, A., & Van Heijst, H. J. (2016). SP12RTS: a degree-12 model of shear-and compressional-wave velocity for Earth's mantle. *Geophysical Journal International*, 204(2), 1024-1039.
38. Krischer, L., T. Megies, R. Barsch, M. Beyreuther, T. Lecocq, C. Caudron, and J. Wassermann (2015), ObsPy: A bridge for seismology into the scientific Python ecosystem, *Computational Science & Discovery* , 8 (1), 014,003.

39. Krischer, L., Hutko, A., van Driel, M., Stähler, S., Bahavar, M., Trabant, C., and Nissen-Meyer, T. (2017). On-demand custom broadband synthetic seismograms, *Seismol. Res. Lett.* 88, no. 4, <https://doi.org/10.1785/0220160210>.
40. Krüger, F., Weber, M., Scherbaum, F., & Schlittenhardt, J. (1993). Double beam analysis of anomalies in the core-mantle boundary region. *Geophysical research letters*, 20(14), 1475-1478.
41. Kustowski, B., Ekström, G., & Dziewoński, A. M. (2008). Anisotropic shear-wave velocity structure of the Earth's mantle: A global model. *Journal of Geophysical Research: Solid Earth*, 113(B6).
42. Lai, H., Garnero, E. J., Grand, S. P., Porritt, R. W., & Becker, T. W. (2019). Global Travel Time Data Set From Adaptive Empirical Wavelet Construction. *Geochemistry, Geophysics, Geosystems*.
43. Landès, M., Hubans, F., Shapiro, N.M., Paul, A. & Campillo, M., 2010. Origin of deep ocean microseisms by using teleseismic body waves, *J. geophys. Res.*, **115**, B05302, doi:10.1029/2009JB006918.
44. Lay, T., & Helmberger, D. V. (1983). A lower mantle S-wave triplication and the shear velocity structure of D". *Geophysical Journal of the Royal Astronomical Society*, 75(3), 799-837.
45. Lay, T., 2007a, Deep earth structure – lower mantle and D , in *Treatise on Geophysics, Seismology and structure of the Earth*, eds Romanowicz, B., Dziewonski, A. & Schubert, G., p. 634, AGU.

46. Lay, T., & Garnero, E. J. (2011). Deep mantle seismic modeling and imaging. *Annual Review of Earth and Planetary Sciences*, 39, 91-123.
47. Lay, T. (2015). Deep Earth Structure: Lower Mantle and D", *Treatise on Geophysics*, 2nd edition, Volume 1, Article 1.22, Oxford, Elsevier, 683-72
48. Lekic, V., Cottaar, S., Dziewonski, A., & Romanowicz, B. (2012). Cluster analysis of global lower mantle tomography: A new class of structure and implications for chemical heterogeneity. *Earth and Planetary Science Letters*, 357, 68-77.
49. Li, Y., Miller, M. S., & Sun, D. (2019). Seismic imaging the D "region beneath the Central Atlantic. *Physics of the Earth and Planetary Interiors*, 292, 76-86.
50. Li, L., Boué, P., & Campillo, M. (2020). Observation and explanation of spurious seismic signals emerging in teleseismic noise correlations. *Solid Earth*, 11, 173-184.
51. Lin, F. C., Tsai, V. C., Schmandt, B., Duputel, Z., & Zhan, Z. (2013). Extracting seismic core phases with array interferometry. *Geophysical Research Letters*, 40(6), 1049-1053.
52. Longuet-Higgins, M. S. (1950). A theory of the origin of microseisms. *Phil. Trans. R. Soc. Lond. A*, 243(857), 1-35.
53. Mégnin, C., & Romanowicz, B. (2000). The three-dimensional shear velocity structure of the mantle from the inversion of body, surface and higher-mode waveforms. *Geophysical Journal International*, 143(3), 709-728.

54. Moulik, P., & Ekström, G. (2014). An anisotropic shear velocity model of the Earth's mantle using normal modes, body waves, surface waves and long-period waveforms. *Geophysical Journal International*, 199(3), 1713-1738.
55. Nishida, K. (2013). Global propagation of body waves revealed by cross-correlation analysis of seismic hum. *Geophysical Research Letters*, 40(9), 1691-1696.
56. Nishida, K., & Takagi, R. (2016). Teleseismic S wave microseisms. *Science*, 353(6302), 919-921.
57. Nissen-Meyer, T., Driel, M. V., Stähler, S., Hosseini, K., Hempel, S., Auer, L., ... & Fournier, A. (2014). AxiSEM: broadband 3-D seismic wavefields in axisymmetric media. *Solid Earth*, (1), 425-445.
58. Panning, M., & Romanowicz, B. (2006). A three-dimensional radially anisotropic model of shear velocity in the whole mantle. *Geophysical Journal International*, 167(1), 361-379.
59. Phạm, T. S., Tkalčić, H., Sambridge, M., & Kennett, B. L. (2018). Earth's correlation wavefield: late coda correlation. *Geophysical Research Letters*, 45(7), 3035-3042.
60. Poli, P., Pedersen, H. A., & Campillo, M. (2012). Emergence of body waves from cross-correlation of short period seismic noise. *Geophysical Journal International*, 188(2), 549-558.
61. Poli, P., Campillo, M., Pedersen, H., & LAPNET Working Group. (2012). Body-wave imaging of Earth's mantle discontinuities from ambient seismic noise. *Science*, 338(6110), 1063-1065.

62. Poli, P., Thomas, C., Campillo, M., & Pedersen, H. A. (2015). Imaging the D "reflector with noise correlations. *Geophysical Research Letters*, 42(1), 60-65.
63. Poli, P., Campillo, M., & de Hoop, M. (2017). Analysis of intermediate period correlations of coda from deep earthquakes. *Earth and Planetary Science Letters*, 477, 147-155.
64. RESIF. (1995). RESIF-RLBP French Broad-band network, RESIF-RAP strong motion network and other seismic stations in metropolitan France. RESIF - Réseau Sismologique et géodésique Français. <https://doi.org/10.15778/resif.fr>
65. Retailleau, L., Boué, P., Stehly, L., & Campillo, M. (2017). Locating microseism sources using spurious arrivals in intercontinental noise correlations. *Journal of Geophysical Research: Solid Earth*, 122(10), 8107-8120.
66. Retailleau, L. and Gualtieri, L., 2019. Toward High-Resolution Period-Dependent Seismic Monitoring of Tropical Cyclones. *Geophysical Research Letters*, 46(3), pp.1329-1337.
67. Ritsema, J., Deuss, A. A., Van Heijst, H. J., & Woodhouse, J. H. (2011). S40RTS: a degree-40 shear-velocity model for the mantle from new Rayleigh wave dispersion, teleseismic traveltimes and normal-mode splitting function measurements. *Geophysical Journal International*, 184(3), 1223-1236.
68. Rost, S., & Earle, P. S. (2010). Identifying regions of strong scattering at the core–mantle boundary from analysis of PKKP precursor energy. *Earth and Planetary Science Letters*, 297(3-4), 616-626.

69. Ruigrok, E., Campman, X., & Wapenaar, K. (2011). Extraction of P-wave reflections from microseisms. *Comptes Rendus Geoscience*, 343(8-9), 512-525.
70. Sabra, K. G., Gerstoft, P., Roux, P., Kuperman, W. A., & Fehler, M. C. (2005). Extracting time-domain Green's function estimates from ambient seismic noise. *Geophysical Research Letters*, 32(3).
71. Sager, K., Ermert, L., Boehm, C., & Fichtner, A. (2018). Towards full waveform ambient noise inversion. *Geophysical Journal International*, 212(1), 566-590.
72. Sager, K., Boehm, C., Ermert, L., Krischer, L., & Fichtner, A. (2018). Sensitivity of seismic noise correlation functions to global noise sources. *Journal of Geophysical Research: Solid Earth*.
73. Shapiro, N. M., & Campillo, M. (2004). Emergence of broadband Rayleigh waves from correlations of the ambient seismic noise. *Geophysical Research Letters*, 31(7)
74. Shapiro, N. M., Campillo, M., Stehly, L., & Ritzwoller, M. H. (2005). High-resolution surface-wave tomography from ambient seismic noise. *Science*, 307(5715), 1615-1618.
75. Snieder, R. (2004). Extracting the Green's function from the correlation of coda waves: A derivation based on stationary phase. *Physical Review E*, 69(4), 046610.
76. Stutzmann, E., Ardhuin, F., Schimmel, M., Mangeney, A., & Patau, G. (2012). Modelling long-term seismic noise in various environments. *Geophysical Journal International*, 191(2), 707-722.

77. Swiss Seismological Service (SED) at ETH Zurich (1983), National seismic networks of Switzerland; ETH Zurich, doi:10.12686/sed/networks/ch, other/Seismic Network.
78. Scherbaum, F., Krüger, F., & Weber, M. (1997). Double beam imaging: mapping lower mantle heterogeneities using combinations of source and receiver arrays. *Journal of Geophysical Research: Solid Earth*, 102(B1), 507-522.
79. Simmons, N. A., Forte, A. M., & Grand, S. P. (2009). Joint seismic, geodynamic and mineral physical constraints on three-dimensional mantle heterogeneity: Implications for the relative importance of thermal versus compositional heterogeneity. *Geophysical Journal International*, 177(3), 1284-1304.
80. Slovenian Environment Agency (2001). Seismic network of the Republic of Slovenia, Ljubljana, Slovenia: International Federation of Digital Seismograph Networks. <https://doi.org/10.7914/SN/SL>, other/Seismic Network.
81. Tkalčić, H., Young, M., Muir, J. B., Davies, D. R., & Mattesini, M. (2015). Strong, multi-scale heterogeneity in Earth's lowermost mantle. *Scientific reports*, 5, 18416.
82. Tkalčić, H., & Phạm, T. S. (2018). Shear properties of Earth's inner core constrained by a detection of J waves in global correlation wavefield. *Science*, 362(6412), 329-332.
83. Thomas, C., Garnero, E. J., & Lay, T. (2004). High-resolution imaging of lowermost mantle structure under the Cocos plate. *Journal of Geophysical Research: Solid Earth*, 109(B8).

84. Thomas, C., Kendall, J. M., & Lowman, J. (2004). Lower-mantle seismic discontinuities and the thermal morphology of subducted slabs. *Earth and Planetary Science Letters*, 225(1-2), 105-113.
85. Wang, S., & Tkalčić, H. (2020). Seismic Event Coda-Correlation: Towards Global Coda-Correlation Tomography. *Journal of Geophysical Research: Solid Earth*.
86. Weber, M., & Körnig, M. (1992). A search for anomalies in the lowermost mantle using seismic bulletins. *Physics of the earth and planetary interiors*, 73(1-2), 1-28.
87. Williams, Q., & Garnero, E. J. (1996). Seismic evidence for partial melt at the base of Earth's mantle. *Science*, 273(5281), 1528-1530.
88. Workman, R. K., & Hart, S. R. (2005). Major and trace element composition of the depleted MORB mantle (DMM). *Earth and Planetary Science Letters*, 231(1), 53-72.
89. Wu, B., Xia, H., Wang, T., & Shi, X. (2018). Simulation of core phases from coda interferometry. *Journal of Geophysical Research: Solid Earth*.
90. Wysession, M. E., Lay, T., Revenaugh, J., Williams, Q., Garnero, E. J., Jeanloz, R., & Kellogg, L. H. (1998). The D "discontinuity and its implications. The core-mantle boundary region, 28, 273-297.
91. Yao, Y., Whittaker, S., & Thorne, M. S. (2015). D "discontinuity structure beneath the North Atlantic from Scd observations. *Geophysical Research Letters*, 42(10), 3793-3801.

92. Zhan, Z., Ni, S., Helmberger, D. V., & Clayton, R. W. (2010). Retrieval of Moho-reflected shear wave arrivals from ambient seismic noise. *Geophysical Journal International*, 182(1), 408-420.
93. Zhang, J., Gerstoft, P., & Bromirski, P. D. (2010). Pelagic and coastal sources of P-wave microseisms: Generation under tropical cyclones. *Geophysical Research Letters*, 37, L15301. <https://doi.org/10.1029/2010GL044288>